

# Surface-growing organophosphorus layer on layered double hydroxides enables boosted and durable electrochemical freshwater/seawater oxidation



Shunfa Zhou<sup>a</sup>, Jiatang Wang<sup>a</sup>, Jing Li<sup>a</sup>, Liyuan Fan<sup>b</sup>, Zhao Liu<sup>a</sup>, Jiawei Shi<sup>a</sup>, Weiwei Cai<sup>a,\*</sup>

<sup>a</sup> Hydrogen Energy Technology, Innovation Center of Hubei Province, Faculty of Materials Science and Chemistry, China University of Geosciences, Wuhan 430074, China

<sup>b</sup> College of Science and Engineering, James Cook University, 1 James Cook Drive, Townsville, QLD 4811, Australia

## ARTICLE INFO

### Keywords:

Oxygen evolution reaction  
Organophosphorus layer  
Self-growing  
Physical blocking  
Electrostatic repelling

## ABSTRACT

Developing high-efficiency and cost-effective electrocatalysts for oxygen evolution reaction (OER) is crucial for hydrogen production from electrolysis. Herein, a facile and universal strategy for fabricating organophosphorus (OP) layer encapsulated layered double hydroxide (LDH) is proposed for robust freshwater/seawater oxidation. This approach is based on a self-growing strategy using phytic acid (PA) to realize superb OER activity due to the electron transfer from metal ions in LDH to the phosphate groups in the OP layer. The phosphate group enriched OP layer can also efficiently avoid chloride corrosion via “physical blocking” and “electrostatic repelling”, enabling the OP-NiCo-LDH catalyst to show durable seawater oxidation catalysis performance. It requires an overpotential of 330 mV to deliver a 500 mA cm<sup>-2</sup> seawater oxidation with excellent durability for 500 h. Moreover, only 1.59 V is required to achieve a 500 mA cm<sup>-2</sup> overall seawater splitting for OP-NiCo-LDH||NiMoN cell. Therefore, this work provides a strategy to design robust OER catalysts for industrial water/seawater electrolysis.

## 1. Introduction

Hydrogen is a promising alternative fuel to fossil fuels due to its high gravimetric energy density and zero-emission property [1–3]. Electrocatalytic water splitting is an efficient pathway for high-purity hydrogen production, which could be powered by renewable electricity from waste heat, intermittent wind or solar energy [4–6]. Typically, water splitting involves two half-reactions, the cathodic hydrogen evolution reaction (HER) and the anodic oxygen evolution reaction (OER) [7,8]. OER is relatively sluggish because of the complicated four-electron transfer process ( $4\text{OH}^- \rightarrow 2\text{H}_2\text{O} + \text{O}_2 + 4\text{e}^-$  in alkaline media), which usually requires a high overpotential and has been considered the primary bottleneck of a water electrolysis technology [9,10]. Over the past decades, numerous efficient and low-cost electrocatalysts have been reported to promote the OER kinetics rate, such as transition metal (TM) oxides [11], hydroxides [12], phosphides [13], nitrides [14], sulphides [15], and selenides [16]. Some of these electrocatalysts even outperform the benchmark Ru/Ir-dioxides ( $\text{RuO}_2$  and  $\text{IrO}_2$ ), which largely invigorates the advancement of electrocatalytic water splitting.

Nevertheless, most of these electrocatalysts focus on the electrolysis of freshwater, a scarce resource in many countries [17]. Unlike freshwater, seawater has several advantages, including nearly unlimited resource reserves and easy combination with sustainable ocean-related electricity-generation technologies, especially in some coastal zones [18]. However, it requires high corrosion-resistive catalysts due to high-concentration chloride anions ( $\text{Cl}^-$ ) in seawater electrolysis. Other than the strong corrosivity,  $\text{Cl}^-$  will form hypochlorite ( $\text{ClO}^-$ ) through the chloride evolution reaction (CLER) at high oxidation potential and compete with OER [19,20]. The theoretical potential of CLER is about 490 mV higher than that of OER at pH= 14, which means that the OER electrocatalysts must work at a low overpotential, e.g., beneath 490 mV to achieve a 100 % selectivity. On the other hand, considering the inevitable corrosion on the electrocatalysts from the ubiquitous and aggressive  $\text{Cl}^-$  in the seawater, developing the high-efficiency electrocatalysts with robust corrosion resistance is still challenging.

In light of the challenging showing above, the outstanding electrocatalysts toward seawater OER are supposed to be qualified by the following factors: i) high intrinsic OER catalytic activity; ii) small

\* Corresponding author.

E-mail addresses: [willcai1985@gmail.com](mailto:willcai1985@gmail.com), [caiww@cug.edu.cn](mailto:caiww@cug.edu.cn) (W. Cai).

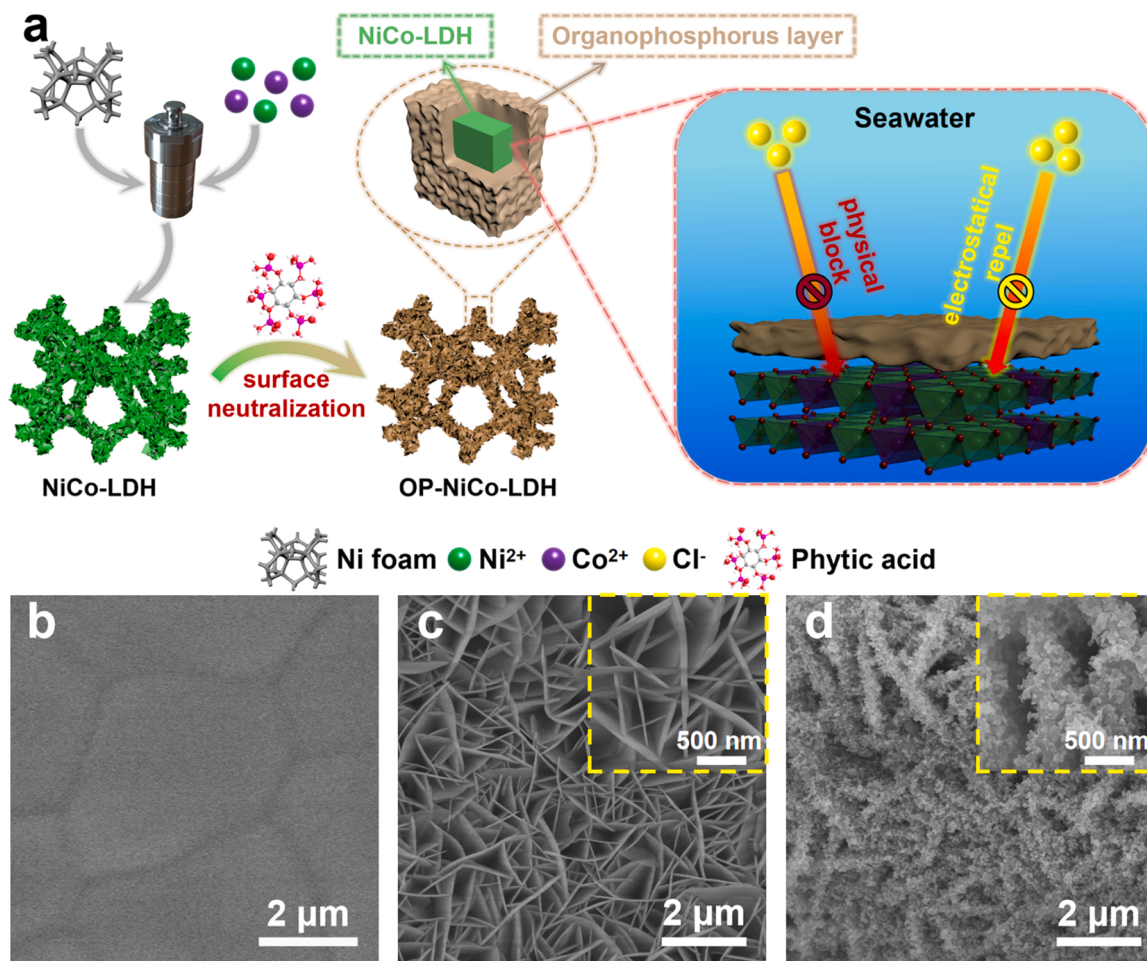


**Fig. 1.** Preparation of the OP-NiCo-LDH catalyst. (a) Schematic illustration for the synthesis steps of the OP-NiCo-LDH catalyst; SEM images of (b) bare Ni foam, (c) NiCo-LDH and (d) OP-NiCo-LDH.

charge-transfer resistance; iii) the ability to deliver usable current density ( $\geq 500 \text{ mA cm}^{-2}$ ) at a low overpotential; iv) good structural stability and strong corrosion resistance to Cl<sup>-</sup>. TM-based and layered double hydroxides (LDHs) have been proven to be the most promising OER electrocatalyst candidates due to their unique two-dimensional layered structure and special physicochemical properties [21,22]. However, the OER performance of LDHs in seawater is still unsatisfactory owing to the inadequate long-term stability in Cl<sup>-</sup>-containing media [23]. According to the up-to-date literature, two strategies have been well known to enhance the stability of electrocatalysts in a Cl<sup>-</sup> containing water oxidation. One is “physical blocking” through designing a Cl<sup>-</sup> blocking layer over the catalysts. For example, Lee et al. [23] fabricated a GO@Fe@Ni-Co@NF electrode with superior Cl<sup>-</sup> corrosion resistance. The graphene oxide overlayed on the catalyst could separate the electrode from seawater, thus protecting the active site from Cl<sup>-</sup> corrosion. Vos et al. [24] reported an IrO<sub>x</sub> electrode covered by a MnO<sub>x</sub> film and demonstrated that the MnO<sub>x</sub> film could be performed as a barrier that prevents Cl<sup>-</sup> from invading the inside IrO<sub>x</sub>. Another method is “electrostatic repelling” through constructing a Cl<sup>-</sup> repelling layer on the catalysts. For instance, Ma et al. [25] demonstrated the existence of SO<sub>4</sub><sup>2-</sup> in the electrolyte that can effectively alleviate the Cl<sup>-</sup> corrosion within anodic alkaline seawater electrolysis. This is attributed to the preferential adsorption of additive SO<sub>4</sub><sup>2-</sup> on the anode surface, which repels Cl<sup>-</sup> adsorption in a bulk phase by electrostatic repulsive force. Balaji et al. reported that a perm-selective polymer (Nafion) on IrO<sub>2</sub>/Ti electrode could repel Cl<sup>-</sup> by electrostatic repulsive forces and achieve a nearly 100 % OER selectivity in a 0.5 M NaCl solution. Above all, it is reasonable to

combine the merits of these two strategies to maximize the performance considering the corrosion resistance of the seawater OER catalysts.

Phytic acid (PA) contains six phosphate groups and is a common product in numerous plants [26]. As reported, PA can significantly enhance the anti-corrosion property of materials in a Cl<sup>-</sup>-rich environments due to its strong chelation ability with metal ions and the corrosion inhibition effect of phosphate ions [27,28]. Furthermore, the abundant phosphate groups can provide sufficient protons, resulting in an adjusted electronic structure of metal sites, which plays an important role in OER catalysis [29,30]. Inspired by the benefits of PA, a facile and universal organophosphorus (OP) layer encapsulation strategy was developed to simultaneously enhance the activity and durability of NiCo-LDH catalyst for efficient oxidation electrocatalysis applied in both fresh water and seawater in this work. The OP layer can be self-assembled on the surface of LDH due to the chelation ability of the PA (Fig. 1a). Notably, the OP layer assembled on the LDH surface can physically block the Cl<sup>-</sup> adsorption due to the compact structure of the OP and repel the Cl<sup>-</sup> adsorption because of the electrostatic interaction between the Cl<sup>-</sup> and phosphate ions. At the same time, the phosphate ions can promote proton transfer during the catalytic OER processing [31] and withdraw electrons from Ni and Co sites, thus enhancing the electrophilicity of metal centers [32]. In addition, the modulated electronic structure has been revealed to promote the intrinsic activity and optimize the Gibbs free energy of intermediates' adsorption on the metal sites, as reported by the experimental and calculation work [33]. Consequently, the results showed that the as-synthesized OP-NiCo-LDH exhibits excellent OER activity and durability in freshwater and

seawater. Applying a reported NiMoN catalyst to the cathodic HER electrode [18], the OP-NiCo-LDH||NiMoN seawater electrolysis cell requires only 1.53 and 1.59 V cell voltages to deliver current densities of 100 and 500 mA cm<sup>-2</sup> overall, respectively. Moreover, it is operated continuously for more than 500 h during the seawater splitting.

## 2. Experimental

### 2.1. Chemicals

Ni foam (NF, thickness: 1 mm; porosity: 96 %; surface density: ~350 g m<sup>-2</sup>) was used as received. Nickel nitrate hexahydrate (Ni (NO<sub>3</sub>)<sub>2</sub>·6 H<sub>2</sub>O, AR), cobalt nitrate hexahydrate (Co(NO<sub>3</sub>)<sub>2</sub>·6 H<sub>2</sub>O, AR), manganese nitrate tetrahydrate (Mn(NO<sub>3</sub>)<sub>2</sub>·4 H<sub>2</sub>O, AR), cetyltrimethylammonium bromide (CTAB, AR, 99 %), phytic acid (AR, 50 % in H<sub>2</sub>O), ethanol (AR, 99.5 %), acetone (AR, 99.5 %), potassium hydroxide (KOH, AR), sodium chloride (NaCl, AR) and hydrochloric acid (HCl, 37 %) were purchased from Aladdin (shanghai, china). All the reagents were used without any further purification. Deionized (DI) water (resistivity: 18.3 MΩ cm) was used to prepare all aqueous solutions.

### 2.2. Synthesis of NF-supported LDHs

Prior to the synthesis, the NF was cleaned with acetone, 1 M HCl and DI water successively to remove the organic contaminant and the oxide layer from the surface. NiCo-LDH on NF was synthesized using a modified hydrothermal reaction based on a previous report [34]. In a typical synthesis, 2.25 mmol Ni(NO<sub>3</sub>)<sub>2</sub>·6 H<sub>2</sub>O, 0.75 mmol Co (NO<sub>3</sub>)<sub>2</sub>·6 H<sub>2</sub>O and 1 g CTAB were dissolved in a mixed solution of methanol (60 mL) and DI water (12 mL) under stirring to form a transparent solution. A piece of NF (3 cm × 7 cm) was put into the above solution and transferred into a 100 mL Teflon-lined stainless-steel autoclave. The autoclave was sealed and maintained at 180 °C for 24 h. The NF-supported NiCo-LDH was obtained by washing with deionized water and ethanol several times and then drying in an oven at 60 °C for 12 h. The fabrication process of NF-supported Co-LDH, Mn-LDH, CoMn-LDH, and NiCoMn-LDH is similar to that of NiCo-LDH by changing the metal salts and their ratios.

### 2.3. Synthesis of OP-LDHs and OP

Typically, 1 mL phytic acid (50 % aqueous solution) was added to 10 mL ethanol. After stirring at room temperature for 10 min, a piece of NF (1 cm × 3 cm) supported NiCo-LDH was immersed into the above solution and heated in a 25 mL Teflon-lined stainless steel autoclave at 100 °C for 6 h. The OP-NiCo-LDH was obtained by washing with deionized water and ethanol several times and then drying in an oven at 60 °C for 6 h. OP-Co-LDH, OP-Mn-LDH, OP-CoMn-LDH and OP-NiCoMn-LDH were prepared through a similar process for OP-NiCo-LDH, except for the use of NF-supported Co-LDH, Mn-LDH, CoMn-LDH and NiCoMn-LDH, respectively. OP was prepared following a similar approach for OP-NiCo-LDH, except for the absence of NF-supported NiCo-LDH. The product was collected by centrifugation.

### 2.4. Synthesis of NF-supported NiMoN

The synthesis procedure for the NiMoN catalyst was based on the previous report [18]. First, 0.582 g Ni(NO<sub>3</sub>)<sub>2</sub>·6 H<sub>2</sub>O and 0.618 g (NH<sub>4</sub>)<sub>6</sub>Mo<sub>7</sub>O<sub>24</sub>·4 H<sub>2</sub>O were dissolved into 50 mL DI water. After stirring, the above solution was transferred into a 100 mL Teflon-lined stainless steel autoclave with a piece of pre-treated NF (2 cm × 5 cm). The autoclave was sealed, and maintained at 150 °C for 6 h. After being cooled to room temperature, the NiMoO<sub>4</sub> on Ni foam was obtained by washing with DI water and then drying in an oven at 60 °C overnight under vacuum. Afterwards, one piece of the as-prepared NiMoO<sub>4</sub>/NF (1 cm<sup>2</sup>) was placed in the middle of a tube furnace and then heated at

500 °C for 1 h under a 120 standard cubic centimeters (sccm) NH<sub>3</sub> and 30 sccm Ar. After the furnace was naturally cooled to room temperature, the NF-supported NiMoN catalyst was obtained.

### 2.5. Physical characterizations

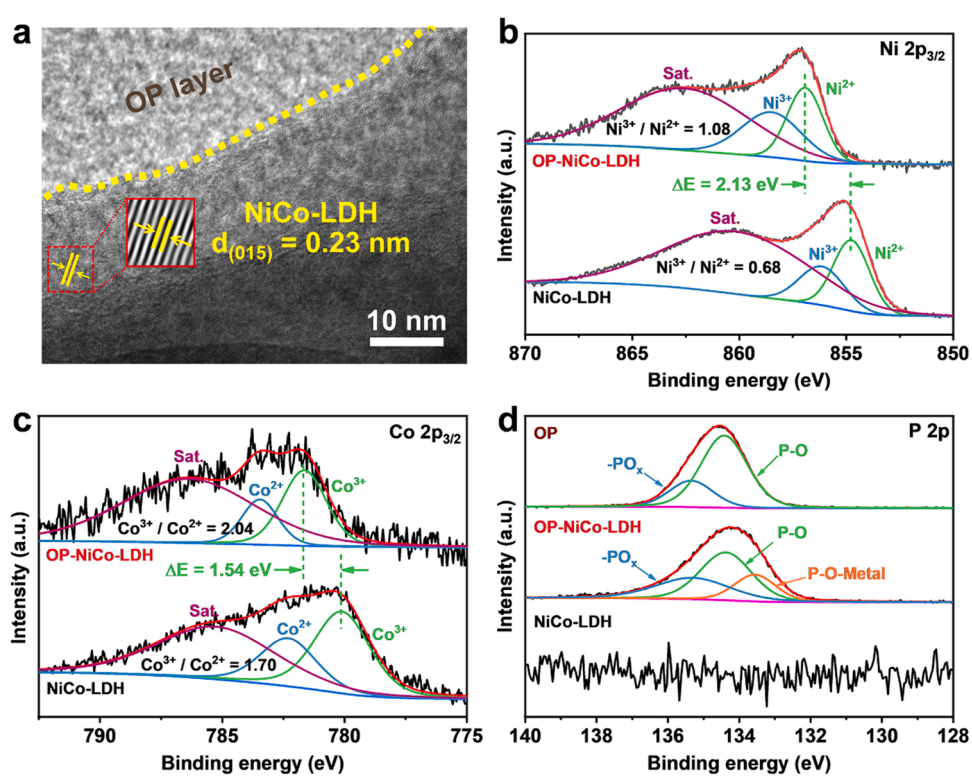
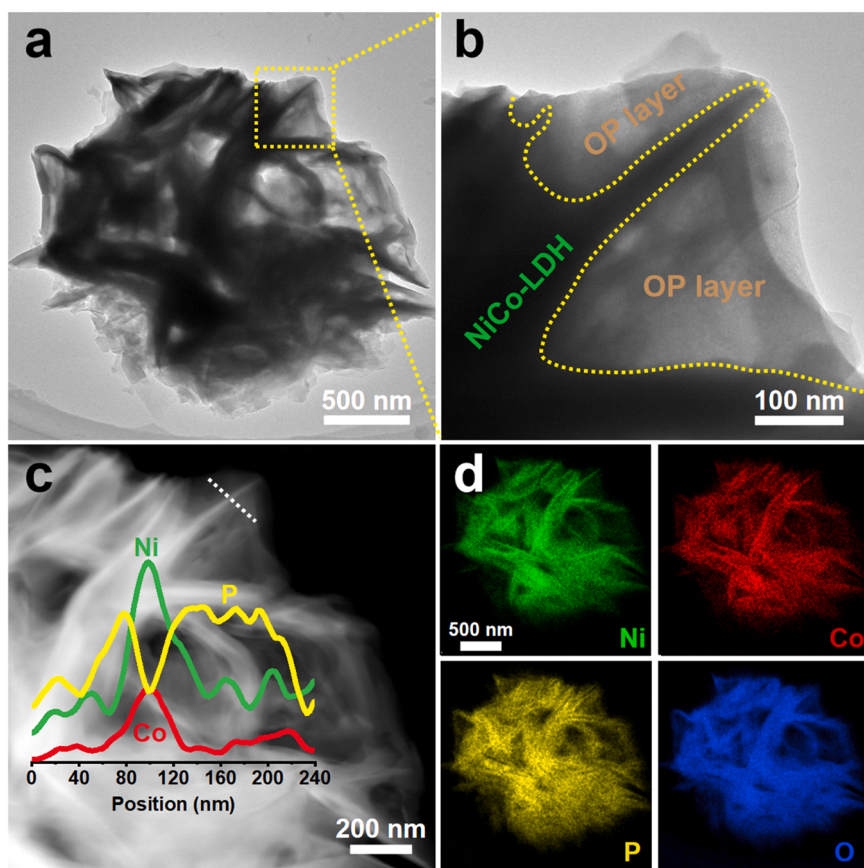
Powder X-ray diffraction patterns were acquired by X-ray diffraction (Bruker AXS D8-Fous, Germany) with Cu-K $\alpha$  radiation. Scanning electron microscopy (SEM, Hitachi SU8000, Japan) and transmission electron microscopy (TEM, Talos F200x, Japan) were used to study the morphology and nanostructure of the samples. Fourier transform infrared spectrometry (FTIR, NEXUS 870, USA) was used to investigate the detailed structure of the samples. X-ray photoelectron spectroscopy (XPS) results were obtained on an Escalab 250XI spectrometer (ThermoFisher, USA). Raman spectra were collected on a Renishaw in the Reflex spectrometer system equipped with a 532 nm laser excitation source. EPR measurements were accomplished at room temperature on an ELEXSYS E500 EPR spectrometer (Bruker, UK). Contact angle measurements were conducted on a contact angle measuring and drop contour analysis system (Dataphysics OCA 20, Germany).

### 2.6. Electrochemical measurements

The catalytic performance of the samples was evaluated on a Gamry Reference 1000 electrochemical station using a three-electrode configuration, which consists of a working electrode (the samples to be tested), a counter electrode (graphite rod) and a reference electrode (Hg/HgO, 1 M KOH). The electrolyte (1 M KOH and 1 M KOH + 0.5 M NaCl) was purged with O<sub>2</sub> for 30 min to ensure it was O<sub>2</sub> saturated before the measurement, and O<sub>2</sub> continued flowing during testing. Cyclic voltammetry tests were performed to activate the catalysts until repeatable curves were obtained. Linear-sweep voltammetry (LSV) measurements were conducted at a rate of 5 mV s<sup>-1</sup> with iR compensation. The recorded potential (E<sub>Hg/HgO</sub>) was calibrated to the reversible hydrogen electrode (RHE) using the equation: E<sub>RHE</sub> = E<sub>Hg/HgO</sub> + 0.098 + 0.0591 × pH. The electrochemically active surface area (ECSA) was estimated by the double-layer capacitance (C<sub>dl</sub>), which was calculated based on the cyclic voltammograms (CV) collected between 20 and 100 mV s<sup>-1</sup> in the range from 1.0 to 1.1 V versus RHE. By plotting the capacitive current at 1.05 V versus RHE against the scan rates, the C<sub>dl</sub> was obtained as half of the corresponding slope, and the ECSA was derived from the equation ECSA = C<sub>dl</sub>/C<sub>s</sub>, where C<sub>s</sub> is the specific capacitance. The C<sub>s</sub> for a flat surface were 20–60 μF cm<sup>-2</sup>, and an adopted value of 40 μF cm<sup>-2</sup> was used to roughly calculate the ECSA. For durability testing, 5000 CV cycles were performed between 1.026 and 1.526 V versus RHE with a scan rate of 100 mV s<sup>-1</sup>, and the corresponding LSV curves were recorded before and after the CV cycles were performed. For comparison, 2 mg commercial IrO<sub>2</sub> was dispersed in ethanol solution with Nafion, and the ink was then dropped by a micropipette on NF. The mass loading of IrO<sub>2</sub> on Ni foam is about 1 mg cm<sup>-2</sup>.

### 2.7. DFT calculations

The density functional theory (DFT) calculations were performed using the Vienna *Ab Initio* Simulation package (VASP). U - J (Ueff) values were set at 3.87 eV for Ni and 3.52 eV for Co. Kohn-Sham wave functions were expanded in a plane wave basis to describe the valence electrons. Electronic exchange and correlation were described by the generalized gradient approximation (GGA) with the Perdew-Burke-Ernzerhof (PBE) functional. The Brillouin zone was sampled with a (3 × 3 × 1) Monkhorst-pack k-point mesh. The kinetic energy cutoff for the computations was set as 500 eV, and the convergence thresholds for energy and force were taken to be 10<sup>-5</sup> eV and 0.02 eV/Å, respectively.



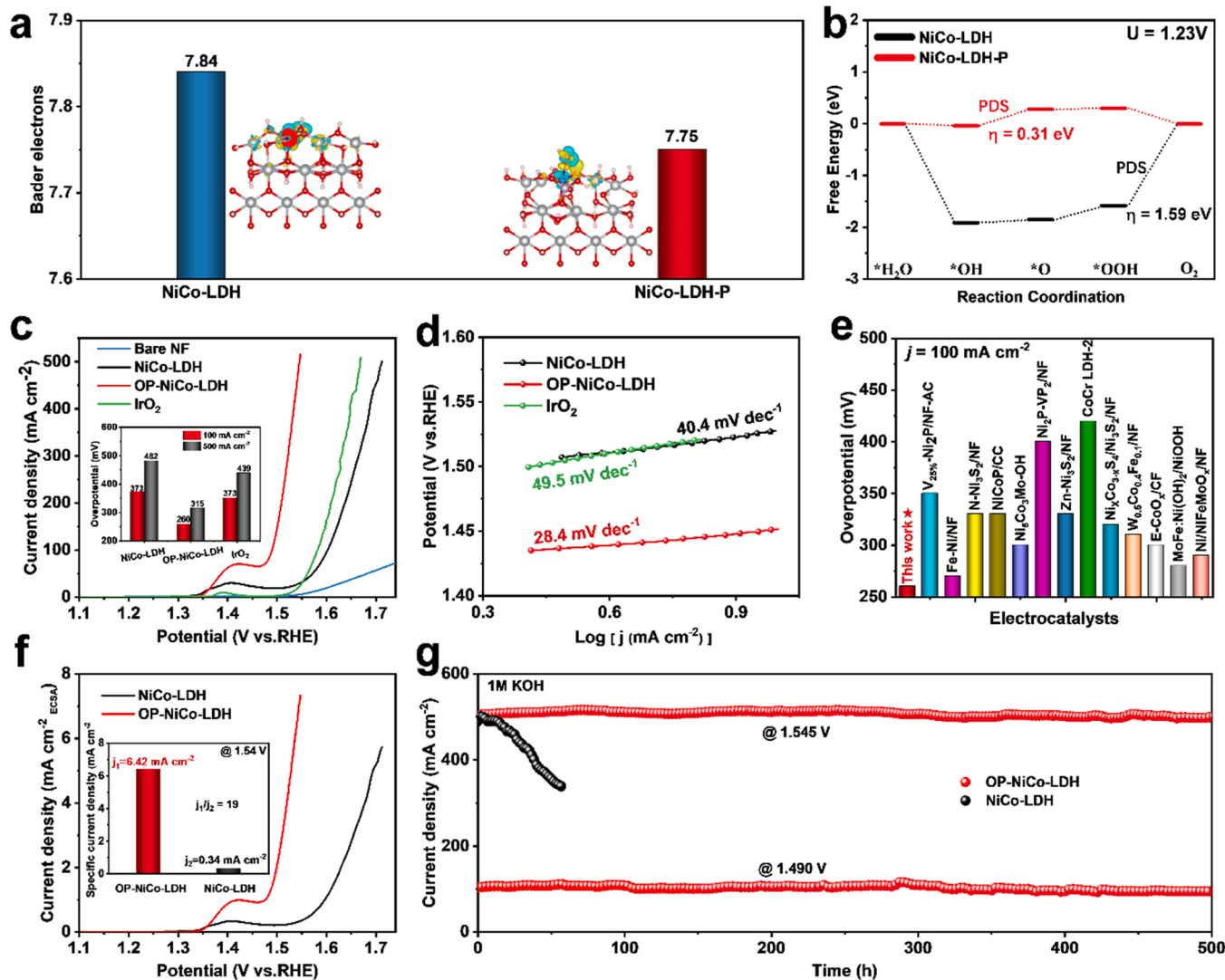


**Fig. 4.** OER performance in freshwater. (a) Bader charges for Co atom in NiCo-LDH and NiCo-LDH-P. The inserts show the side views of charge density differences in NiCo-LDH (left) and NiCo-LDH-P (right). Yellow and cyan regions represent electron accumulation and depletion, respectively. Gray, blue, red, purple and white spheres represent Ni, Co, O, P and H atoms, respectively (b) Free energy diagrams for the OER over NiCo-LDH and NiCo-LDH-P; (c) LSV plots of NiCo-LDH, OP-NiCo-LDH, IrO<sub>2</sub> and bare Ni foam in 1 M KOH electrolyte. The insert in (c) shows the corresponding overpotentials required at 100 and 500 mA cm<sup>-2</sup>; (d) Tafel plots of NiCo-LDH, OP-NiCo-LDH and IrO<sub>2</sub> in 1 M KOH electrolyte; (e) Comparison of overpotentials required at 100 mA cm<sup>-2</sup> with previously reported catalysts (Table S1); (f) ECSA normalized OER activity of NiCo-LDH and OP-NiCo-LDH. The insert compares specific current density at 1.54 V versus RHE; (g) Chronoamperometric curves of NiCo-LDH and OP-NiCo-LDH catalysts at constant current densities of 100 and 500 mA cm<sup>-2</sup> in 1 M KOH electrolyte.

### 3. Results and discussion

#### 3.1. Material synthesis and characterizations

As depicted in Fig. 1a, the OP-NiCo-LDH catalyst was synthesized via two steps. First, a pristine LDH nanosheet array was grown on NF based on a reported procedure[34]. Subsequently, the NiCo-LDH-supported NF was immersed in an ethanol solution of PA for surface-neutralization. During the surface-neutralization process, the compacted OP layer was simultaneously assembled on LDH tightly via a dehydration reaction. Since the catalyst was synthesized with 1 vol% PA solution for surface-neutralization to display the best OER activity (Figs. S1–S2), which was selected as a representative sample denoted as OP-NiCo-LDH in the following discussion. The optical images of NiCo-LDH and OP-NiCo-LDH are presented in Fig. S3. The formation of the OP layer can be visually demonstrated from the color change of NiCo-LDH from light green to dark green after surface neutralization.

Micro-morphology of the catalysts was first tested by SEM. The SEM

images (Fig. 1b and Fig. S4) show that the bare NF has a smooth and flat surface. After the solvothermal process, the NiCo-LDH nanosheets with 50 nm thickness were vertically grown on the NF surface (Fig. 1c). The resulting thickness of the NiCo-LDH nanosheets after surface-neutralization with PA increases remarkably to 100–200 nm due to the formation of the OP layer (Fig. 1d).

TEM image of the NiCo-LDH catalyst (Fig. S5a) displays a transparent feature, indicating the ultrathin nature. The corresponding high-resolution TEM (HR-TEM) image (Fig. S5b) reveals lattice spacing of 0.23 nm and 0.19 nm, which correspond to the crystal faces (015) and (018) of NiCo-LDH, respectively. TEM image (Fig. 2a-b) of OP-NiCo-LDH after the surface-neutralization shows a core-shell structure with the OP layer encapsulated on the NiCo-LDH surface. The core-shell structure was further evaluated by EDX linear scan (Fig. 2c). The results present that the P signal is mainly distributed at the outside shell, while Ni and Co are primarily located in the center parts. Additionally, the high-angle annular dark field scanning transmission electron microscopy (HAADF-STEM) image and the corresponding elemental maps

of OP-NiCo-LDH confirm the uniform distributions of the Ni, Co, O, C and P elements (Fig. 2d and Fig. S6).

Fourier transform infrared spectroscopy (FT-IR) and Raman measurements were also carried out to analyze the composition of the synthesized catalysts. Compared with NiCo-LDH, FT-IR spectra of OP-NiCo-LDH and OP shows similar representative peaks attributed by P = O, P-O-C, PO<sub>4</sub><sup>3-</sup>, P-O-H(M) and OH<sup>-</sup> [35–38], indicating the succussed encapsulation of the OP layer on the surface of the NiCo-LDH (Fig. S7). Furthermore, Raman spectra of both the NiCo-LDH and OP-NiCo-LDH (Fig. S8) show two obvious characteristic peaks at the wavelength of 464.6 and 517 cm<sup>-1</sup> ascribed to the Metal-O bonds of LDH [39]. OP-NiCo-LDH and OP also show similar peaks attributed to the bonds of P-O-C, P-O-H(M), P = O and C-H, which further proves the encapsulation of OP layer.[36,40,41].

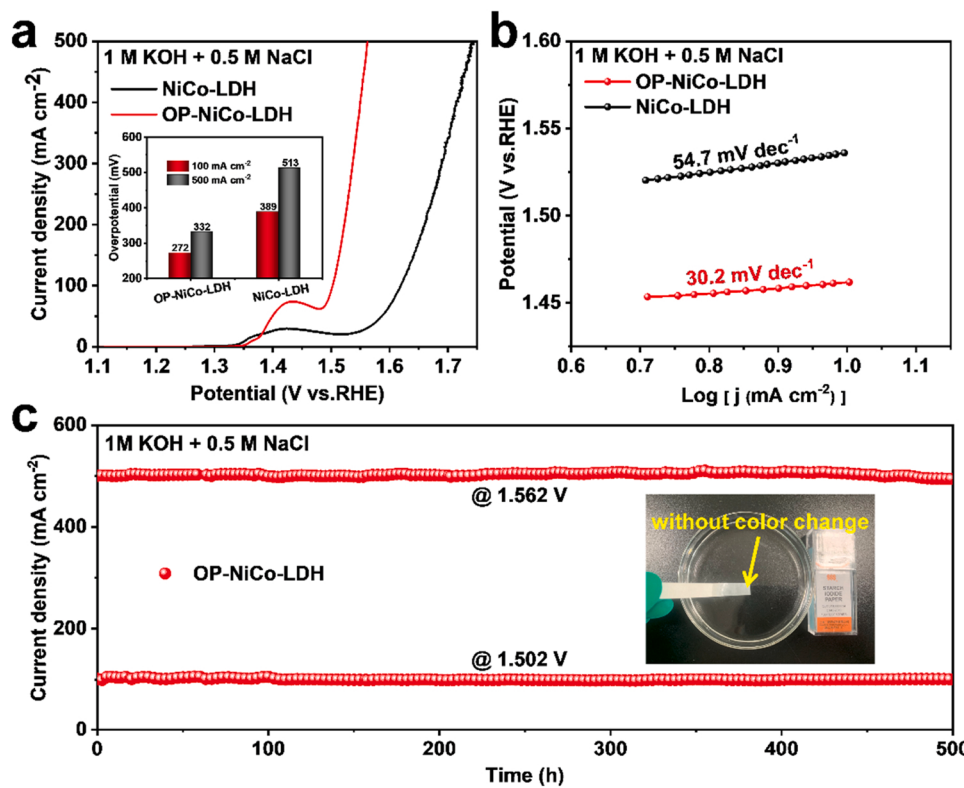
X-ray diffraction (XRD) patterns of OP, NiCo-LDH and OP-NiCo-LDH (Fig. S9) were also conducted. OP has only one wide peak at 20°–30°, which can be recognized as the carbon ring in the PA molecule, indicating the amorphous feature of the OP layer. For NiCo-LDH, the diffraction peaks at 11.2, 22.4, 34.5, and 38.6° can be attributed to the (003), (006), (009) and (015) facets of the LDH phase (JCPDS No. 33-0429), respectively. Compared with NiCo-LDH, the intensity of the diffraction peaks in OP-NiCo-LDH is much lower, which is attributed to the encapsulation of the amorphous OP layer on the surface of NiCo-LDH. Further detection by the HR-TEM image identifies the lattice spacing of 0.23 nm, resulting from the (015) facet of NiCo-LDH (Fig. 3a), confirming that NiCo-LDH was not decomposed during the surface-neutralization process. To characterize the surface chemical composition and bonding configuration of the catalysts, X-ray photoelectron spectroscopy (XPS) analysis was performed. The XPS results of the OP-NiCo-LDH confirm the existence of Ni, Co, O, C and P elements (Fig. S10). The intensity of the C 1 s and O 1 s XPS peaks for OP-NiCo-LDH increase noticeably compared to NiCo-LDH due to the carbon ring and the abundant phosphate groups in PA molecules [42]. Fig. 3b shows the high-resolution Ni 2p<sub>3/2</sub> spectra of NiCo-LDH and OP-NiCo-LDH. Two subpeaks in the NiCo-LDH spectrum at 854.8 and 856.1 eV are assigned to the Ni<sup>2+</sup> and Ni<sup>3+</sup>, respectively, after deconvolution calculation [34]. Compared with NiCo-LDH, the binding energy of Ni 2p<sub>3/2</sub> peak for OP-NiCo-LDH is upshifted by 2.1 eV, which is attributed to the strong electron-withdrawing effect of phosphate groups and the formation of the metal-O-P bond [43]. According to the high-resolution Co 2p spectra (Fig. 3c), peak positions of Co 2p<sub>3/2</sub> for OP-NiCo-LDH (781.7 eV) also shift positively to higher binding energy compared to NiCo-LDH (780.2 eV). These positive shifts of binding energy suggest the lower electron density around metal sites of OP-NiCo-LDH. Furthermore, the specific ratios of Ni<sup>3+</sup>/Ni<sup>2+</sup> and Co<sup>3+</sup>/Co<sup>2+</sup> increase markedly from 0.68 and 1.70 for NiCo-LDH to 1.08 and 2.04 for OP-NiCo-LDH, respectively. The literature studies have revealed that the high-valence Ni or Co species in OER play an essential role in the NiCo-based catalysts because they can accelerate the reaction and provide high intrinsic activity [44,45]. Introducing phosphate groups can promote electron delocalization and electron withdrawal from the Ni/Co sites. The more electrophilic Ni or Co sites would be better at promoting the adsorption of hydroxyls and water molecules on the catalyst surfaces [46]. The high-resolution O1s spectrum of NiCo-LDH can be deconvoluted into three peaks (Fig. S11) corresponding to Metal-O (530.6 eV), OH<sup>-</sup> (531.9 eV) and adsorbed H<sub>2</sub>O (533.9 eV), respectively. Both OP and OP-NiCo-LDH have three types of oxygen species: OH<sup>-</sup> (531.8 eV), P-O/C-O (533.0 eV) and adsorbed H<sub>2</sub>O, which is consistent with the FT-IR and Raman results. Besides, a new peak at 531.2 eV occurs in OP-NiCo-LDH, which is attributed to the Metal-O-P bond [43], suggesting the formation of metal chelate in the OP layer. The asymmetric property of OH<sup>-</sup> in the XPS spectrum indicates that the peak area (OH<sup>-</sup>/Metal-O) can be used to evaluate the amount of oxygen vacancies [47,48]. The ratio of OH/Metal-O in the OP-NiCo-LDH is calculated to be 1.67, which is much higher than that of NiCo-LDH (0.23), indicating that additional oxygen vacancies generated

in OP-NiCo-LDH during the surface-neutralization. The electron paramagnetic resonance (EPR) spectra have been compared in Fig. S12 to provide direct evidence for oxygen vacancies. Compared with the NiCo-LDH, the OP-NiCo-LDH shows a stronger signal at *g* = 2.000, indicating a higher concentration of oxygen vacancies in the OP-NiCo-LDH. It is common sense that oxygen vacancy can accelerate sluggish electrocatalytic reactions [49]. Subpeaks located at 134.4 and 135.4 eV in the P 2p XPS spectra of the NiCo-LDH and the OP-NiCo-LDH (Fig. 3d) are contributed by -PO<sub>x</sub> and P-O in the OP layers. More importantly, the subpeak located at 133.6 eV owing to the metal-O-P bond in the spectrum of OP-NiCo-LDH can be found, further proving the formation of metal chelate on the NiCo-LDH surface via the neutralization reaction. C 1 s XPS spectrum of OP-NiCo-LDH (Fig. S13) shows subpeaks at 284.8 eV and 286.8 eV, which can be attributed to C-C and C-O bonds originating from the organic component in the OP layer.

### 3.2. OER in freshwater

To obtain a deep insight into the influence of phosphate groups on metal sites for OER catalysis, density functional theory (DFT) calculations were performed before electrocatalytic OER measurements. First, the charge transfer change between the phosphate group and the Co site was predicted through the charge density difference analysis, as shown in Fig. 4a. Compared with NiCo-LDH, an obvious electron depletion is observed near the Co atom, revealing the higher oxidation state of Co induced by phosphate groups. Therefore, the electron transfer from the Co ion to the phosphate group is observed, consistent with XPS results. Moreover, Bader charges show that the average electron density of the Co atom of NiCo-LDH-P is 0.09 e, which is lower than that of NiCo-LDH, indicating that the phosphate group can decrease the electron cloud density of Co and results in the electron-poor state of the Co site. This result confirms the strong electron coupling between the metal sites and the phosphate groups. And the local electronic structure of the metal sites can be modulated by this coupling, resulting in an enhanced electrolytic OER activity. The density of states (DOS) is also performed to investigate the intrinsic electronic structure of NiCo-LDH and NiCo-LDH-P (Fig. S14). The phosphate group induces finite DOS change in the electronic states of NiCo-LDH-P in contrast to that of the NiCo-LDH, especially near the Fermi level, which may provide more favorable electronic structures for the adsorption of OER intermediates. The calculated *d*-band center of NiCo-LDH-P (-4.27 eV) shifts to a higher energy than that of NiCo-LDH (-4.66 eV), implying the increased unoccupied antibonding states and thus modified binding strength with adsorbed oxygenated intermediates. Generally, the electronic structure of the catalysts fundamentally dominates their binding strength with surface-adsorbed species. As shown in Fig. 4b, the Gibbs free energy ( $\Delta G$ ) for four elementary reaction steps, which determines the adsorption strength of the OER intermediates, have been calculated. The results show that the formation of \*O<sub>2</sub> is the rate-determining step for NiCo-LDH, while the formation of \*O is the rate-determining step for NiCo-LDH-P. Furthermore, between the two rate-determining steps, the NiCo-LDH-P (0.31 eV) shows much lower energy barriers ( $\Delta G$ ) than that of NiCo-LDH (1.59 eV), indicating that NiCo-LDH-P is more favourable to the OER kinetics. Therefore, the DFT calculations prove that the strong synergistic interactions between the metal sites and the phosphate groups can effectively modify the local electronic structure of the metal sites and alter the adsorption strength of the oxygenated intermediates, yielding a significantly enhanced intrinsic electrocatalytic activity. This implies that the NiCo-LDH-P has excellent potential for the application of efficient OER catalysts.

The electrocatalytic OER performance of these as-prepared catalysts was evaluated in a typical three-electrode cell in O<sub>2</sub>-saturated 1 M KOH solution. Commercial IrO<sub>2</sub> loaded on NF was also tested as a reference for comparison. According to the linear sweep voltammetry (LSV) curves in Fig. 4c, the OP-NiCo-LDH catalyst performed superior



electrocatalytic with an ultra-low overpotential of 260 mV at an OER current density of 100 mA cm<sup>-2</sup>, remarkably lower than those of NiCo-LDH (373 mV) and IrO<sub>2</sub> (351 mV). Compared with NiCo-LDH, OP-NiCo-LDH shows a higher intensity of Ni(II)/Ni(III) redox peak around 1.4 V (vs. RHE) [50], suggesting that the species with more active have been generated after the surface-neutralization [51]. To collect the overpotentials at low current densities, CV tests were carried out (Fig. S15). The OP-NiCo-LDH catalyst exhibited superb catalytic activity with an overpotential of 222 mV at 10 mA cm<sup>-2</sup>, much lower than NiCo-LDH (298 mV). The Tafel slope of OP-NiCo-LDH is about 28.4 mV dec<sup>-1</sup>, lower than 40.4 and 49.5 mV dec<sup>-1</sup> observed from NiCo-LDH and IrO<sub>2</sub>, respectively (Fig. 4d). The smaller Tafel slope suggests the improved OER kinetics on OP-NiCo-LDH. The OP-NiCo-LDH catalyst also outperforms the most reported non-precious catalysts (Fig. 4e and Table S1). Besides, the OP-NiCo-LDH catalyst can deliver a higher current density of 500 mA cm<sup>-2</sup> at the competitive overpotential of 315 mV, significantly lower than that of NiCo-LDH (482 mV) and IrO<sub>2</sub> (439 mV). Electrochemical impedance spectroscopy (EIS) measurements were conducted to evaluate the charge transfer resistance ( $R_{ct}$ ) during the OER process on the catalysts (Fig. S16 and Table S2). It can be found that the  $R_{ct}$  of OP-NiCo-LDH (1.82 Ω) is much smaller than that of NiCo-LDH (4.35 Ω) and bare NF (5.33 Ω), as desired because the phosphate groups in the OP layer can promote proton transfer during OER. To assess the intrinsic activity of OP-NiCo-LDH, LSV curves were normalized by electrochemical active surface area (ECSA, Fig. S17) for OP-NiCo-LDH and NiCo-LDH (Fig. 4 f). The specific current density of OP-NiCo-LDH is 6.42 mA cm<sup>-2</sup> at 1.54 V (vs. RHE), which is ca. 19 times as high as that of NiCo-LDH (0.34 mA cm<sup>-2</sup>), demonstrating the former one's ultrahigh intrinsic activity.

Before the durability measurement, the contact angle (Fig. S18a-c) was tested to investigate the surface property and mass transfer properties of the OP-NiCo-LDH catalyst. The results of both NiCo-LDH and OP-NiCo-LDH show a hydrophilic feature but in contrast with bare NF. The super hydrophilicity of OP-NiCo-LDH results from the abundant phosphate groups in the OP layer. Literature studies have demonstrated

**Fig. 5.** OER performance in seawater. (a) LSV plots of NiCo-LDH and OP-NiCo-LDH in 1 M KOH + 0.5 M NaCl electrolyte. The inset shows the corresponding overpotentials required at 100 and 500 mA cm<sup>-2</sup>; (b) Tafel plots of NiCo-LDH and OP-NiCo-LDH in 1 M KOH + 0.5 M NaCl electrolyte; (c) CP curves of OP-NiCo-LDH catalysts at constant current densities of 100 and 500 mA cm<sup>-2</sup> in 1 M KOH + 0.5 M NaCl electrolyte. The inset shows the potassium iodide starch paper immersed in the electrolyte after a 500-h durability test.

that a hydrophilic surface is beneficial for accelerating electrolyte diffusion and intimate contact between the electrolyte and catalysts [52]. Besides, gas bubble release easily at the surface of the catalyst is also important for the OER performance because the generated bubbles will block the active sites and hinder reactions [13,53]. Therefore, the aerophobic properties of the catalysts were also investigated in this study. As depicted in Fig. S18d-f, OP-NiCo-LDH demonstrates a larger bubble contact angle (150°) than those of NiCo-LDH (145°) and bare NF (143°), indicating that OP-NiCo-LDH is relatively more aerophobic. Therefore, the produced O<sub>2</sub> bubbles during the OER process can be released quickly from the surface of the OP-NiCo-LDH catalyst. As a result, the OP-NiCo-LDH catalyst is expected to perform superior electrocatalytic stability toward the OER, as revealed in Fig. 4g operating continuously for about 500 h at 100 and 500 mA cm<sup>-2</sup> in 1 M KOH without any current loss. But on the contrary, the current density of NiCo-LDH declines sharply within 60 h from 500 mA cm<sup>-2</sup> to 300 mA cm<sup>-2</sup>. This good long-term stability of OP-NiCo-LDH may be contributed by the protection effect and the aerophobic feature of the OP layer. The surface-neutralization strategy is another relevant factor for improving the OER performance of other TM-LDHs (Fig. S19-S22).

### 3.3. OER in simulated seawater

After considering the superior OER performance of OP-NiCo-LDH in 1 M KOH electrolyte, the catalytic activity was further evaluated in 1 M KOH + 0.5 M NaCl for simulated seawater oxidation. The most crucial challenge for electrochemical seawater splitting is to prevent the formation of hypochlorite via ClOR, which will compete with the OER process and cause anodic corrosion. The OP-NiCo-LDH catalyst requires an overpotential of 315 mV to reach a current density at 500 mA cm<sup>-2</sup>, which lowers the potential to the theoretical potential of ClOR. As shown in Fig. 5a and Fig. S23, the OER activity of OP-NiCo-LDH slightly declines due to the invitation of Cl<sup>-</sup>, which is the main consequence of the blocking of some catalytic sites by the Cl<sup>-</sup> [18,54]. It should be noted that the decline of OER activity for NiCo-LDH is more significant than

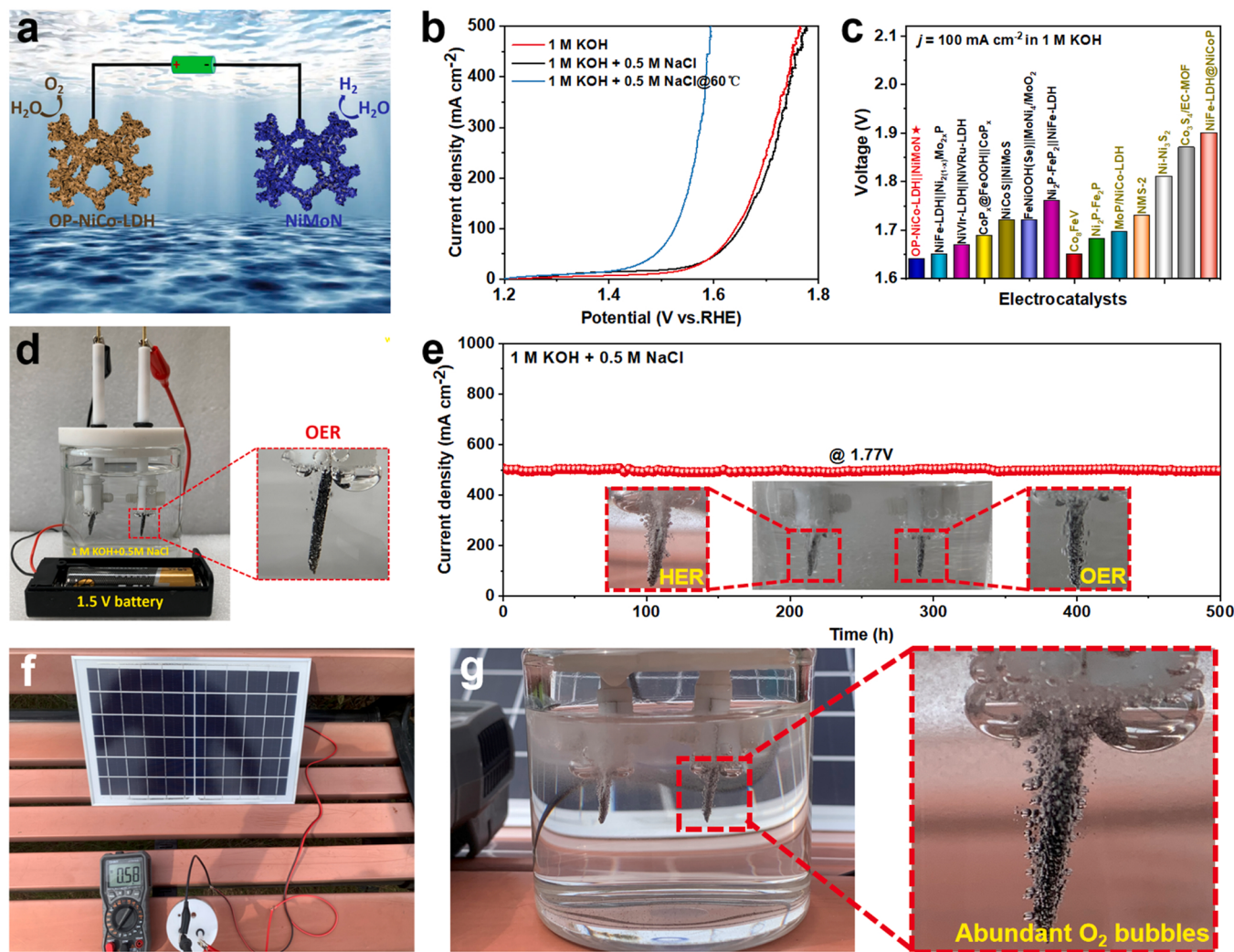


**Fig. 6.** Overall seawater splitting performance. (a) Schematic illustration of overall seawater splitting electrolyzer using OP-NiCo-LDH anode and NiMoN cathode; (b) LSV plots for the OP-NiCo-LDH||NiMoN electrolyzer in different electrolytes; (c) Voltages required to reach  $100 \text{ mA cm}^{-2}$  overall water electrolysis for the OP-NiCo-LDH||NiMoN electrolyzer and other self-supported catalysts in 1 M KOH electrolyte (Brown labels represent bifunctional catalysts); (d) Photo of the OP-NiCo-LDH||NiMoN electrolyzer driven by a 1.5 V battery in 1 M KOH + 0.5 M NaCl electrolyte; (e) Long-term stability test of the OP-NiCo-LDH||NiMoN coupled electrolyzer at room temperature with a constant current density of  $500 \text{ mA cm}^{-2}$  in 1 M KOH + 0.5 M NaCl electrolyte. (f) Photo of the OP-NiCo-LDH||NiMoN coupled electrolyzer driven by a silicon solar cell in 1 M KOH + 0.5 M NaCl electrolyte and (g) corresponding photos of the generated bubbles on the working OP-NiCo-LDH||NiMoN electrolyzer.

that of OP-NiCo-LDH. This proves that the OP layer on the catalyst surface can efficiently enhance the ability to block the ubiquitous and aggressive  $\text{Cl}^-$ . Specifically, the OP-NiCo-LDH catalyst requires overpotentials of 272 and 332 mV to reach  $100 \text{ mA cm}^{-2}$  and  $500 \text{ mA cm}^{-2}$  seawater oxidation, respectively. As shown in Fig. S24, the OP-NiCo-LDH catalyst also displayed a superior catalytic activity with the overpotential of 232 mV at  $10 \text{ mA cm}^{-2}$ , better than NiCo-LDH (310 mV). Moreover, the corresponding Tafel slope (Fig. 5b) and the charge transfer resistance (Fig. S25 and Table S3) of OP-NiCo-LDH ( $30.2 \text{ mV dec}^{-1}$  and  $2.79 \Omega$ ) are smaller than that of NiCo-LDH ( $54.7 \text{ mV dec}^{-1}$  and  $9.91 \Omega$ ), indicating the fast kinetics and charge transfer when with OP layers. The OP-NiCo-LDH catalyst outperforms the most recently reported catalysts (Table S4). The durability of the seawater oxidation catalyzed by the OP-NiCo-LDH catalyst was measured using the accelerated cyclic voltammetry (CV) cycling test and chronoamperometry (CP) methods. As shown in Fig. S26, the LSV curves obtained before and after 5000 CV cycles are mostly overlapped in both 1 M KOH and 1 M KOH + 0.5 M NaCl electrolytes. Moreover, SEM images after 5000 CV cycles in 1 M KOH + 0.5 M NaCl show that the micro-morphology of OP-NiCo-LDH is well-kept, indicating its excellent

structural stability (Fig. S27). Although surface construction can be detected, the thickness of the nanosheet changing is not obvious, indicating that the protective effect of the OP layer is sustained. In addition, XPS analysis was carried out to characterize the surface composition change of OP-NiCo-LDH after the stability test. The high-resolution Co 2p<sub>3/2</sub> and Ni 2p<sub>3/2</sub> XPS spectra show that the ratios of both  $\text{Ni}^{3+}/\text{Ni}^{2+}$  and  $\text{Co}^{3+}/\text{Co}^{2+}$  increase dramatically due to the transformation of hydroxide to oxyhydroxide during the OER process (Fig. S28). The O 1s XPS spectra of OP-NiCo-LDH shows that the amount of M-O species in the catalyst increase after the OER process, which is related to the generation of -OOH species (Fig. S29a) [55]. The P 2p XPS spectra of OP-NiCo-LDH after OER verifies that the phosphate groups are well retained after OER (Fig. S29b). The Raman spectrum of OP-NiCo-LDH after 5000 CV cycles shows two broad peaks corresponding to -OOH species (Fig. S30), indicating the bond formation of Metal-OOH, the intermediate product during OER [56,57]. CP curves (Fig. 5c) show that the OP-NiCo-LDH could work continuously for 500 h at a stable performance of a current density of  $100 \text{ mA cm}^{-2}$  and  $500 \text{ mA cm}^{-2}$  in the simulated seawater condition with concentrated  $\text{Cl}^-$ . As shown in Fig. S31, the Faraday efficiency of OP-NiCo-LDH is close to 100 %,

indicating that no side reactions occur during the OER process. Besides, the electrolyte after the CP measurement was examined by potassium iodide starch paper and shows that color change was not observed (inset of Fig. 5c), suggesting the excellent OER selectivity and anti-corrosion ability during the seawater oxidation. The exceptional corrosion resistance ability can be attributed to the combined blocking and repelling effect of the OP layer to Cl<sup>-</sup> [27,28].

To examine the practical potential of the OP-NiCo-LDH catalyst in cell application, a specified seawater electrolysis cell was fabricated by pairing the OP-NiCo-LDH anode with the NiMoN cathode [18], as schematically illustrated in Fig. 6a. The LSV curves of the OP-NiCo-LDH||NiMoN cell show an excellent overall water-splitting performance in both 1 M KOH and the simulated seawater electrolytes (Fig. 6b). Specifically, the cell voltages required to reach 100 and 500 mA cm<sup>-2</sup> current densities are as low as 1.64 and 1.76 V, respectively. These achieved voltages are much lower than those of the IrO<sub>2</sub>||Pt/C cell (Fig. S32). On the other hand, the cell voltage to achieve a current density of 100 mA cm<sup>-2</sup> during freshwater splitting has outperformed the most previously reported catalysts (Fig. 6c and Table S2). However, when considering the Cl<sup>-</sup> contribution, the OP-NiCo-LDH||NiMoN cell performance slightly declines. The electrolysis cell requires 1.65 and 1.78 V cell voltage to yield current densities of 100 and 500 mA cm<sup>-2</sup>, respectively. In addition, the cell voltage to deliver 100 mA cm<sup>-2</sup> OER decreases significantly to 1.53 V when increasing the operating temperature from room temperature to 60 °C (Fig. 6b and Fig. S33), which is typically applied in industrial water electrolysis devices. Interestingly, a 1.5 V battery can power the OP-NiCo-LDH||NiMoN electrolysis cell in the simulated seawater, and plenty of small bubbles emerging from the anode can be observed (Fig. 6d). The long-term durability of the OP-NiCo-LDH||NiMoN cell was also measured at a constant cell voltage (Fig. 6e), and it can keep working stably for 500 h at 500 mA cm<sup>-2</sup> in simulated seawater electrolytes with no current density reduction. Finally, a commercial Si PV module was applied to power the OP-NiCo-LDH||NiMoN seawater electrolysis cell (Fig. 6f). The OP-NiCo-LDH||NiMoN cell achieves a current of 0.58 A (surface area: 1 cm<sup>2</sup>), and abundant bubbles have been generated from the surface of both electrodes (Fig. 6g), indicating the feasibility and efficient water splitting cooperated with the solar cell system.

#### 4. Conclusion

In summary, a facile and universal surface-neutralization approach has been developed to enhance the catalytic OER activity of TM-LDH-based catalysts using a self-assembly OP layer encapsulation strategy. Experimental results and DFT calculations verify that the phosphate groups can modulate the electron structure of metal centers and enhance the sluggish OER kinetics. In addition to the enhanced intrinsic activity, the improved OER performance can be attributed to the high ratio of high-valence state metal species induced by the phosphate groups, a small charge-transfer resistance, a hydrophilic feature for electrolyte diffusion and easy bubble release ability. Most importantly, the phosphate groups-enriched OP layer can separate metal sites from Cl<sup>-</sup> via simultaneously “physical blocking” and “electrostatic repelling”. Thus, the OP-NiCo-LDH catalyst displays an excellent OER performance in freshwater and seawater electrolytes. The further fabricated OP-NiCo-LDH||NiMoN electrolysis cell requires 1.59 V applied voltage to deliver 500 mA cm<sup>-2</sup> overall seawater splitting and showed robust stability at an industrial current density of 500 mA cm<sup>-2</sup> for 500 h continuous operation. This work provides a deep insight into designing OER electrocatalysts with excellent activity and stability for industrial seawater splitting.

#### CRediT authorship contribution statement

**Shunfa Zhou:** Conceptualization, Methodology, Writing – original draft. **Jiatang Wang:** Data curation, Writing – original draft. **Jing Li:**

Supervision Writing – review & editing, Funding acquisition. **Liyuan Fan:** Writing – review & editing. **Zhao Liu:** Writing – review & editing. **Jiawei Shi:** Software, Validation. **Weiwei Cai:** Conceptualization, Supervision Writing – review & editing, Funding acquisition.

#### Declaration of Competing Interest

The authors declare that they have no known competing financial interests or personal relationships that could have appeared to influence the work reported in this paper.

#### Data availability

Data will be made available on request.

#### Acknowledgements

We are grateful for financial support from the National Natural Science Foundation of China (No. 22179121), Knowledge Innovation Program of Wuhan-Basic Research (2022010801010202) and Research Fund Program of Guangdong Provincial Key Laboratory of Fuel Cell Technology (FC202201).

#### Appendix A. Supporting information

Supplementary data associated with this article can be found in the online version at doi:10.1016/j.apcatb.2023.122749.

#### References

- [1] C.-T. Dinh, A. Jain, F.P.G. de Arquer, P. De Luna, J. Li, N. Wang, X. Zheng, J. Cai, B. Z. Gregory, O. Voznyy, B. Zhang, M. Liu, D. Sinton, E.J. Crumlin, E.H. Sargent, Multi-site electrocatalysts for hydrogen evolution in neutral media by destabilization of water molecules, *Nat. Energy* 4 (2018) 107–114.
- [2] X.X. Zou, Y. Zhang, Noble metal-free hydrogen evolution catalysts for water splitting, *Chem. Soc. Rev.* 44 (2015) 5148–5180.
- [3] L.L. Guo, J.Q. Chi, J.W. Zhu, T. Cui, J.P. Lai, L. Wang, Dual-doping NiMoO<sub>4</sub> with multi-channel structure enable urea-assisted energy-saving H<sub>2</sub> production at large current density in alkaline seawater, *Appl. Catal. B* 320 (2023), 121977.
- [4] L. Li, P. Wang, Q. Shao, X. Huang, Metallic nanostructures with low dimensionality for electrochemical water splitting, *Chem. Soc. Rev.* 49 (2020) 3072–3106.
- [5] Y.T. Luo, Z.Y. Zhang, M. Chhowalla, B.L. Liu, Recent advances in design of electrocatalysts for high-current-density water splitting, *Adv. Mater.* 34 (2022) 18.
- [6] J. Yan, L. Kong, Y. Ji, J. White, Y. Li, J. Zhang, P. An, S. Liu, S.T. Lee, T. Ma, Single atom tungsten doped ultrathin alpha-Ni(OH)<sub>2</sub> for enhanced electrocatalytic water oxidation, *Nat. Commun.* 10 (2019) 2149.
- [7] B. Zhu, D. Xia, R. Zou, Metal-organic frameworks and their derivatives as bifunctional electrocatalysts, *Coord. Chem. Rev.* 376 (2018) 430–448.
- [8] L. Yan, B. Zhang, J.L. Zhu, Y.Y. Li, P. Tsakarlas, P.K. Shen, Electronic modulation of cobalt phosphide nanosheet arrays via copper doping for highly efficient neutral-pH overall water splitting, *Appl. Catal. B* 265 (2020), 118555.
- [9] B. Zhang, X.L. Zheng, O. Voznyy, R. Comin, M. Bajdich, M. Garcia-Melchor, L. L. Han, J.X. Xu, M. Liu, L.R. Zheng, F.P.G. de Arquer, C.T. Dinh, F.J. Fan, M. J. Yuan, E. Yassitepe, N. Chen, T. Regier, P.F. Liu, Y.H. Li, P. De Luna, A. Jammohamed, H.L.L. Xin, H.G. Yang, A. Vojvodic, E.H. Sargent, Homogeneously dispersed multimetal oxygen-evolving catalysts, *Science* 352 (2016) 333–337.
- [10] N.T. Suen, S.F. Hung, Q. Quan, N. Zhang, Y.J. Xu, H.M. Chen, Electrocatalysis for the oxygen evolution reaction: recent development and future perspectives, *Chem. Soc. Rev.* 46 (2017) 337–365.
- [11] M.P. Browne, Z. Sofer, M. Pumera, Layered and two dimensional metal oxides for electrochemical energy conversion, *Energy Environ. Sci.* 12 (2019) 41–58.
- [12] M.J. Liu, K.A. Min, B. Han, L.Y.S. Lee, Interfacing or doping? Role of Ce in highly promoted water oxidation of nife-layered double hydroxide, *Adv. Energy Mater.* 11 (2021), 2101281.
- [13] L.C. Huang, R.Q. Yao, X.Q. Wang, S. Sun, X.X. Zhu, X.H. Liu, M.G. Kim, J.S. Lian, F. Z. Liu, Y.Q. Li, H.X. Zong, S. Han, X.D. Ding, In situ phosphating of Zn-doped bimetallic skeletons as a versatile electrocatalyst for water splitting, *Energy Environ. Sci.* 15 (2022) 2425–2434.
- [14] Y. Yang, R. Zeng, Y. Xiong, F.J. DiSalvo, H.D. Abruna, Cobalt-based nitride-core oxide-shell oxygen reduction electrocatalysts, *J. Am. Chem. Soc.* 141 (2019) 19241–19245.
- [15] D.C. Nguyen, D.T. Tran, T.L.L. Doan, D.H. Kim, N.H. Kim, J.H. Lee, Rational design of core/shell structured Co<sub>3</sub>@Cu<sub>2</sub>Mo<sub>3</sub>S<sub>4</sub> hybridized MoS<sub>2</sub>/N,S-codoped graphene as advanced electrocatalyst for water splitting and Zn-air battery, *Adv. Energy Mater.* 10 (2020), 1903289.
- [16] S. Ni, H.N. Qu, Z.H. Xu, X.Y. Zhu, H.F. Xing, L. Wang, J.M. Yu, H.Z. Liu, C.M. Chen, L.R. Yang, Interfacial engineering of the NiSe<sub>2</sub>/FeSe<sub>2</sub> p-p heterojunction for

- promoting oxygen evolution reaction and electrocatalytic urea oxidation, *Appl. Catal. B* 299 (2021), 120638.
- [17] H.J. Chen, Y.H. Zou, J. Li, K.W. Zhang, Y.Z. Xia, B. Hui, D.J. Yang, Wood aerogel-derived sandwich-like layered nanoelectrodes for alkaline overall seawater electrosplitting, *Appl. Catal. B* 293 (2021), 120215.
- [18] L. Yu, Q. Zhu, S. Song, B. McElhenney, D. Wang, C. Wu, Z. Qin, J. Bao, Y. Yu, S. Chen, Z. Ren, Non-noble metal-nitride based electrocatalysts for high-performance alkaline seawater electrolysis, *Nat. Commun.* 10 (2019) 5106.
- [19] W. Zang, T. Sun, T. Yang, S. Xi, M. Waqar, Z. Kou, Z. Lyu, Y.P. Feng, J. Wang, S. J. Pennycook, Efficient hydrogen evolution of oxidized Ni-N3 defective sites for alkaline freshwater and seawater electrolysis, *Adv. Mater.* 33 (2021), e2003846.
- [20] H. You, D. Wu, D. Si, M. Cao, F. Sun, H. Zhang, H. Wang, T.F. Liu, R. Cao, Monolayer NiIr-layered double hydroxide as a long-lived efficient oxygen evolution catalyst for seawater splitting, *J. Am. Chem. Soc.* 144 (2022) 9254–9263.
- [21] J.F. Yu, Q. Wang, D. O'Hare, L.Y. Sun, Preparation of two dimensional layered double hydroxide nanosheets and their applications, *Chem. Soc. Rev.* 46 (2017) 5950–5974.
- [22] Y.H. Tang, Q. Liu, L. Dong, H.B. Wu, X.Y. Yu, Activating the hydrogen evolution and overall water splitting performance of NiFe LDH by cation doping and plasma reduction, *Appl. Catal. B* 266 (2020), 118627.
- [23] A.R. Jadhav, A. Kumar, J. Lee, T. Yang, S. Na, J. Lee, Y. Luo, X. Liu, Y. Hwang, Y. Liu, H. Lee, Stable complete seawater electrolysis by using interfacial chloride ion blocking layer on catalyst surface, *J. Mater. Chem. A* 8 (2020) 24501–24514.
- [24] J.G. Vos, T.A. Wezendonk, A.W. Jeremiassie, M.T.M. Koper, MnO<sub>x</sub>/IrO<sub>x</sub> as selective oxygen evolution electrocatalyst in acidic chloride solution, *J. Am. Chem. Soc.* 140 (2018) 10270–10281.
- [25] T.F. Ma, W.W. Xu, B.R. Li, X. Chen, J.J. Zhao, S.S. Wan, K. Jiang, S.X. Zhang, Z. F. Wang, Z.Q. Tian, Z.Y. Lu, L. Chen, The critical role of additive sulfate for stable alkaline seawater oxidation on nickel-based electrodes, *Angew. Chem. Int. Ed.* 60 (2021) 22740–22744.
- [26] Q. Hu, G. Li, X. Liu, B. Zhu, X. Chai, Q. Zhang, J. Liu, C. He, Superhydrophilic phytic-acid-doped conductive hydrogels as metal-free and binder-free electrocatalysts for efficient water oxidation, *Angew. Chem. Int. Ed.* 58 (2019) 4318–4322.
- [27] L. Yohai, M. Vázquez, M.B. Valcarce, Phosphate ions as corrosion inhibitors for reinforcement steel in chloride-rich environments, *Electrochim. Acta* 102 (2013) 88–96.
- [28] F. Cao, J. Wei, J. Dong, W. Ke, The corrosion inhibition effect of phytic acid on 20SiMn steel in simulated carbonated concrete pore solution, *Corros. Sci.* 100 (2015) 365–376.
- [29] Y. Shao, X. Xiao, Y.P. Zhu, T.Y. Ma, Single-crystal cobalt phosphate nanosheets for biomimetic oxygen evolution in neutral electrolytes, *Angew. Chem. Int. Ed.* 58 (2019) 14599–14604.
- [30] Y.B. Li, C. Zhao, Enhancing water oxidation catalysis on a synergistic phosphorylated nife hydroxide by adjusting catalyst wettability, *ACS Catal.* 7 (2017) 2535–2541.
- [31] P.F. Liu, X. Li, S. Yang, M.Y. Zu, P. Liu, B. Zhang, L.R. Zheng, H. Zhao, H.G. Yang, Ni<sub>2</sub>P(O)/Fe<sub>2</sub>P(O) interface can boost oxygen evolution electrocatalysis, *ACS Energy Lett.* 2 (2017) 2257–2263.
- [32] B.S. Yeo, A.T. Bell, Enhanced activity of gold-supported cobalt oxide for the electrochemical evolution of oxygen, *J. Am. Chem. Soc.* 133 (2011) 5587–5593.
- [33] Z. Li, Q. Wang, X. Bai, M. Wang, Z. Yang, Y. Du, G.E. Sterbinsky, D. Wu, Z. Yang, H. Tian, F. Pan, M. Gu, Y. Liu, Z. Feng, Y. Yang, Doping-modulated strain control of bifunctional electrocatalysis for rechargeable zinc-air batteries, *Energy Environ. Sci.* 14 (2021) 5035–5043.
- [34] J. Jiang, A. Zhang, L. Li, L. Ai, Nickel-cobalt layered double hydroxide nanosheets as high-performance electrocatalyst for oxygen evolution reaction, *J. Power Sources* 278 (2015) 445–451.
- [35] P. Li, Z. Jin, J. Yang, Y. Jin, D. Xiao, Highly active 3D-nanoarray-supported oxygen-evolving electrode generated from cobalt-phytate nanoplates, *Chem. Mater.* 28 (2015) 153–161.
- [36] X. Chen, G. Zeng, T. Gao, Z. Jin, Y. Zhang, H. Yuan, D. Xiao, In situ formation of high performance Ni-phytate on Ni-foam for efficient electrochemical water oxidation, *Electrochim. Commun.* 74 (2017) 42–47.
- [37] X. Zhou, H. Huang, R. Zhu, R. Chen, X. Sheng, D. Xie, Y. Mei, Green modification of graphene oxide with phytic acid and its application in anticorrosive water-borne epoxy coatings, *Prog. Org. Coat.* 143 (2020), 105601.
- [38] A. Zajac, L. Dyminska, J. Lorenc, S.M. Kaczmarek, G. Leniec, M. Ptak, J. Hanuza, Spectroscopic properties and molecular structure of copper phytate complexes: IR, Raman, UV-Vis, EPR studies and DFT calculations, *J. Biol. Inorg. Chem.* 24 (2019) 11–20.
- [39] J. Hu, C. Zhang, L. Jiang, H. Lin, Y. An, D. Zhou, M.K.H. Leung, S. Yang, Nanohybridization of MoS<sub>2</sub> with layered double hydroxides efficiently synergizes the hydrogen evolution in alkaline media, *Joule* 1 (2017) 383–393.
- [40] P. Godlewska, A. Matraszek, S.M. Kaczmarek, H. Fuks, T. Skibinski, K. Hermanowicz, M. Ptak, I. Szczyciel, L. Macalik, R. Lisiecki, W. Ryba-Romanowski, J. Hanuza, Structural, optical and EPR studies of NaCe(PO<sub>3</sub>)<sub>4</sub> metaphosphate doped with Cr<sup>3+</sup>, *J. Lumin.* 146 (2014) 342–350.
- [41] R. Gond, D.K. Singh, M. Eswaramoorthy, P. Barpanda, Sodium cobalt metaphosphate as an efficient oxygen evolution reaction catalyst in alkaline solution, *Angew. Chem. Int. Ed.* 58 (2019) 8330–8335.
- [42] Y.J. Zhang, T.T. Gao, Z.Y. Jin, X.J. Chen, D. Xiao, A robust water oxidation electrocatalyst from amorphous cobalt-iron bimetallic phytate nanostructures, *J. Mater. Chem. A* 4 (2016) 15888–15895.
- [43] Y.T. Liu, L. Tang, J. Dai, J. Yu, B. Ding, Promoted electrocatalytic nitrogen fixation in Fe-Ni layered double hydroxide arrays coupled to carbon nanofibers: the role of phosphorus doping, *Angew. Chem. Int. Ed.* 59 (2020) 13623–13627.
- [44] H. Sun, L. Chen, Y. Lian, W. Yang, L. Lin, Y. Chen, J. Xu, D. Wang, X. Yang, M. H. Rummerli, J. Guo, J. Zhong, Z. Deng, Y. Jiao, Y. Peng, S. Qiao, Topotactically transformed polygonal mesopores on ternary layered double hydroxides exposing under-coordinated metal centers for accelerated water dissociation, *Adv. Mater.* 32 (2020), e2006784.
- [45] J.X. Kang, X.Y. Qiu, Q. Hu, J. Zhong, X. Gao, R. Huang, C.Z. Wan, L.M. Liu, X. F. Duan, L. Guo, Valence oscillation and dynamic active sites in monolayer NiCo hydroxides for water oxidation, *Nat. Catal.* 4 (2021) 1050–1058.
- [46] Y. Li, Z. Wang, J. Hu, S. Li, Y. Du, X. Han, P. Xu, Metal-organic frameworks derived interconnected bimetallic metaphosphate nanoarrays for efficient electrocatalytic oxygen evolution, *Adv. Funct. Mater.* 30 (2020).
- [47] M. Fang, D. Han, W.B. Xu, Y. Shen, Y. Lu, P. Cao, S. Han, W. Xu, D. Zhu, W. Liu, J. C. Ho, Surface-guided formation of amorphous mixed-metal oxyhydroxides on ultrathin MnO<sub>2</sub> nanosheet arrays for efficient electrocatalytic oxygen evolution, *Adv. Energy Mater.* 10 (2020), 2001059.
- [48] L. Wu, L. Yu, Q. Zhu, B. McElhenney, F. Zhang, C. Wu, X. Xing, J. Bao, S. Chen, Z. Ren, Boron-modified cobalt iron layered double hydroxides for high efficiency seawater oxidation, *Nano Energy* 83 (2021), 105838.
- [49] L. Gao, X. Cui, C.D. Sewell, J. Li, Z. Lin, Recent advances in activating surface reconstruction for the high-efficiency oxygen evolution reaction, *Chem. Soc. Rev.* 50 (2021) 8428–8469.
- [50] Y. Bai, Y. Wu, X. Zhou, Y. Ye, K. Nie, J. Wang, M. Xie, Z. Zhang, Z. Liu, T. Cheng, C. Gao, Promoting nickel oxidation state transitions in single-layer NiFeB hydroxide nanosheets for efficient oxygen evolution, *Nat. Commun.* 13 (2022) 6094.
- [51] T. Zhao, X. Shen, Y. Wang, R.K. Hocking, Y. Li, C. Rong, K. Dastafkan, Z. Su, C. Zhao, In situ reconstruction of V-doped Ni<sub>2</sub>P pre-catalysts with tunable electronic structures for water oxidation, *Adv. Funct. Mater.* 31 (2021), 2100614.
- [52] A. Nairan, C.W. Liang, S.W. Chiang, Y. Wu, P.C. Zou, U. Khan, W.D. Liu, F.Y. Kang, S.J. Guo, J.B. Wu, C. Yang, Proton selective adsorption on Pt-Ni nano-thorn array electrodes for superior hydrogen evolution activity, *Energy Environ. Sci.* 14 (2021) 1594–1601.
- [53] D.J. Zhou, P.S. Li, X. Lin, A. McKinley, Y. Kuang, W. Liu, W.F. Lin, X.M. Sun, X. Duan, Layered double hydroxide-based electrocatalysts for the oxygen evolution reaction: identification and tailoring of active sites, and superaerophobic nanoarray electrode assembly, *Chem. Soc. Rev.* 50 (2021) 8790–8817.
- [54] L. Yu, L. Wu, B. McElhenney, S. Song, D. Luo, F. Zhang, Y. Yu, S. Chen, Z. Ren, Ultrafast room-temperature synthesis of porous S-doped Ni/Fe (oxy)hydroxide electrodes for oxygen evolution catalysis in seawater splitting, *Energy Environ. Sci.* 13 (2020) 3439–3446.
- [55] M. Han, N. Wang, B. Zhang, Y. Xia, J. Li, J. Han, K. Yao, C. Gao, C. He, Y. Liu, Z. Wang, A. Seifitokaldani, X. Sun, H. Liang, High-valent nickel promoted by atomically embedded copper for efficient water oxidation, *ACS Catal.* 10 (2020) 9725–9734.
- [56] X. Luo, P. Ji, P. Wang, X. Tan, L. Chen, S. Mu, Spherical Ni<sub>3</sub>S<sub>2</sub>/Fe-NiP<sub>x</sub> magic cube with ultrahigh water/seawater oxidation efficiency, *Adv. Sci.* 9 (2022), e2104846.
- [57] Z. Qiu, C.W. Tai, G.A. Niklasson, T. Edvinsson, Direct observation of active catalyst surface phases and the effect of dynamic self-optimization in NiFe-layered double hydroxides for alkaline water splitting, *Energy Environ. Sci.* 12 (2019) 572–581.